Journal of Materials Chemistry A

Accepted Manuscript

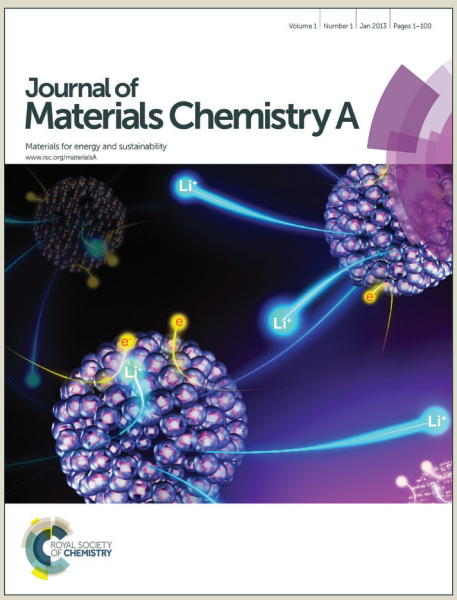

ROYAL SOCIETY OF CHEMISTRY

www.rsc.org/materialsA

Journal of Materials Chemistry A RSCPublishing

ARTICLE

Beyond Conventional Electrocatalysts: Hollow Nanoparticles for Improved and Sustainable Oxygen Reduction Reaction Activity

Cite this: DOI: 10.1039/x0xx00000x

Received 00th January 2012,
Accepted 00th January 2012

DOI: 10.1039/x0xx00000x

www.rsc.org/

Laetitia Dubau,[a, b, *] Miguel Lopez-Haro,[a, b, c] Julien Durst,[d] Laure Guétaz,[e] Pascale Bayle-Guillemaud,[e] Marian Chatenet,[a, b ,f] and Frédéric Maillard[a, b, *]

Long-term catalytic performance of electrode materials is a well-established research priority in electrochemical energy conversion and storage systems, such as proton-exchange membrane fuel cells. Despite extensive efforts in research and development, Pt-based nanoparticles remain the only – but unstable – electrocatalyst able to accelerate efficiently the rate of the oxygen reduction reaction. This paper describes the synthesis and the atomic-scale characterization of hollow Pt-rich/C nanocrystallites, which achieve 4-fold and 5-fold enhancement in specific activity for the oxygen reduction reaction over standard solid Pt/C nanocrystallites of the same size in liquid electrolyte and during real proton-exchange membrane fuel cell (PEMFC) testing, respectively. More importantly, the hollow nanocrystallites can sustain this level of performance during accelerated stress tests, therefore opening new perspectives for the design of improved PEMFC cathode materials.

Introduction

Metallic nanoparticles are widely used in heterogeneous catalysis to accelerate chemical reactions or direct them towards a specific product, thereby minimizing the energetic cost of the catalytic conversion. When precious metals are used, high values of the dispersion are required to increase the mass activity (MA, A g^{-1}_{metal}), and thus decrease the cost of the catalyst. This approach proved particularly successful in proton-exchange membrane fuel cells (PEMFCs), where the replacement of platinum (Pt) blacks, used in early PEMFCs, by carbon-supported Pt nanoparticles has significantly improved the Pt specific power density. Yet, the widespread commercialization of PEMFCs requires a further 10-fold decrease of the materials cost (*i.e.* the anode and cathode catalysts, the catalyst layer ionomer, the proton-exchange membrane, and the bipolar plates). The Pt-based catalysts used in standard PEMFC electrodes constitute a significant fraction of this cost, [1-4] in particular at the cathode, where Pt remains the only durable material able to catalyse efficiently the electrochemical oxygen reduction reaction (ORR). Since 90 % of the atoms are exposed at the surface of a 1 nanometre-sized cuboctahedral Pt particle, [5] the cost issue could be alleviated by reducing the size of the nanoparticles. However, the increased adsorption strength of oxygenated species on the smallest nanocrystallites lowers their intrinsic catalytic activity for the ORR [5, 6] and their stability (the Gibbs-Thompson equation leads to both increased driving force and faster kinetics of dissolution for the smallest Pt nanocrystallites) [7]. Experimental studies suggest that an optimal crystallite size of *ca*. 4-5 nm is required both for improved ORR catalytic activity and stability [2, 6-9]. Improving the ORR mass activity is currently best achieved with homogeneous Pt-M/C nanoalloys (M being a transition metal, M = Co, Ni, Cu or Fe) [1, 4, 10-17] or core-shell nanoparticles composed of a Pt-enriched shell and a metallic or alloyed core [18-21]. The presence of the non-noble transition metal allows binding oxygenated species 0.2 to 0.3 eV weaker than pure Pt, [10, 22] thereby enhancing the ORR rate. A further increase in catalytic activity has been observed with size, shape and composition-controlled Pt-M/C nanoparticles [15, 17, 23-25]. Unfortunately, whatever the initial atomic composition or the catalyst architecture, bimetallic Pt-M/C electrocatalysts feature continuous dissolution of M atoms during PEMFC operation [9, 13, 15, 26-40]. The loss of M atoms causes (i) a decreased catalytic activity of the cathode electrocatalyst, [13, 30, 33, 35, 37, 39] (ii) the depreciation of the H^+/O_2 mass-transport properties of the catalytic layer ionomer/proton exchange membrane (PEM) [37, 41] and (iii) the formation of radical species in the PEM [41, 42]. Even nanostructured bimetallic Pt-M thin films, which are composed of large crystallites do not prevent the dissolution of the less noble element [43]. Therefore, the dilemma of achieving cost-competitive, highly active (platinum-group metal mass normalized) and robust electrocatalysts is still unsolved yet.

In this context, recent studies performed in real PEMFC operating conditions (solid polymer electrolyte, T = 343 or 353 K) [33, 38, 39] have shown that the complete dissolution of M atoms from homogeneously alloyed Pt-M electrocatalysts leads to hollow Pt/C nanoparticles (*i.e.* containing a void in their centre) due to a nanoscale Kirkendall effect. The Kirkendall effect is a vacancy-mediated diffusion mechanism in binary Pt-M alloys or core-shell materials driven by the faster interdiffusion of one element relative to the other [44-48]. At a PEMFC cathode, the faster interdiffusion and the surface segregation of M atoms is driven by their oxophilicity [29, 33, 49]. The net flow of M atoms is then compensated by an opposite flow of vacancies, which generates several nanoscale voids [33]. These vacancies ultimately coalesce into a single void in the centre of the particle, and yield the formation of hollow Pt nanoparticles [33, 38, 50]. The hollow Pt nanocrystallites possess numerous advantages over solid† Pt-M nanocrystallites: (i) increased specific surface area per mass *i.e.* increased number of catalytic sites per gram of Pt, [51] (ii) contracted lattice parameter, [36, 38, 51, 52] (iii) no loss of M^{z+} cations in PEMFC operating conditions, and (iv) low concentration of low coordination sites that strongly bind oxygenated species [53]. As first shown by Wang *et al.*, [51] such characteristics improve the ORR specific activity (SA, μA cm^{-2}_{Pt}). Furthermore, as a 12 nm hollow Pt/C nanoparticle with 8 monolayer thick Pt shell possesses a comparable surface area-to-volume ratio as a 5 nm solid Pt/C nanoparticle, these electrocatalysts are also interesting from the mass activity viewpoint [51]. However, due to the technical complexity of the synthesis procedures (sequential two-step procedure, absence of oxygen), [36, 51, 52] and the presence of residual ligands or metallic salts in the synthesized catalysts, [54-57] only small quantities of hollow Pt-rich/C nanoparticles were produced and the potential of this class of electrocatalysts in real PEMFC conditions remains unknown.

Here, we describe the one-pot surfactant-free synthesis of hollow Pt_xNi_{1-x}/C nanocrystallites with low Ni content. Using a unique combination of high angle annular dark field scanning transmission electron microscopy (HAADF-STEM), electron energy loss spectroscopy (EELS), X-ray diffraction (XRD) and Synchrotron X-ray absorption spectroscopy measurements (XAS), we shed fundamental light into their mechanism of formation and describe their physicochemical characteristics. Their electrocatalytic activity was evaluated in liquid electrolyte and in PEM fuel cell, and compared *vs.* that of standard solid Pt/C electrodes.

Experimental

A. Materials

Reference electrocatalyst

Pt nanoparticles supported on Vulcan XC72® with a weight fraction (wt. %) of 20 % were purchased from E-TeK, and used as a reference material. The number-averaged and the surface-averaged Pt nanoparticle size of the reference Pt/C electrocatalysts are 2.82 ± 0.07 and 3.10 ± 0.07 nm, respectively. The electrocatalyst was used as-received without any further treatment.

Synthesis of hollow PtxNi1-x/C nanoparticles

The hollow Pt_xNi_{1-x}/C nanoparticles were synthesized using an in-house synthesis procedure adapted from the study of Bae *et al.* [12]. In a typical synthesis, 0.46 mmol of $Pt(NH_3)_4Cl_2$ (Alfa Aesar, Specpure) and $NiCl_2$(6 H_2O) (Fluka, > 98.0 %) were first mixed with 0.30 g Vulcan XC72R® (Cabot), 10 mL of ethanol and 250 mL of de-ionized water (Millipore). An aqueous solution of $NaBH_4$ (Aldrich 99.99 % - 5.5 mmol, 0.22 M) was then added at a rate of 5 ml min^{-1} and stirred for 1 h under magnetic stirring at room temperature (293 ± 2 K). The resulting mixture was filtered, thoroughly washed by de-ionized water and dried for 45 minutes at T = 383 K, yielding hollow Pt-Ni/C nanocrystallites. A fraction of this powder was then acid-treated for 12 h in a stirred 1 M H_2SO_4 solution at T = 293 K. This sample is referred to as the Pt-Ni/C-AT electrocatalyst.

B. Physical measurements

X-ray Diffraction Measurements

The synthesized and reference electrocatalysts were analysed using a PANalytical X'Pert Pro MPD vertical goniometer/diffractometer equipped with a diffracted-beam monochromator using Cu(K_a mean) radiation (λ = 0.15418 nm) operating at 45 kV and 40 mA. The 2θ angle extended from 10 to 125° and varied using a step size of 0.033° accumulating data for 525s. The lattice contraction was estimated from the position of the (111), (220) and the (311) diffraction peaks on the reference Pt/C and the synthesized PtxNi1-x/C materials. The average XRD crystallite size, d_{XRD}, was obtained from a fit of the Pt(220) peak using the Debye–Scherrer equation.

X-ray Absorption Spectroscopy Measurements

The X-ray absorption spectroscopy experiments were carried out at the BM30B beamline of the European Synchrotron Radiation Facility (ESRF) in Grenoble. All samples were measured in both transmission and fluorescence mode at the Pt L_3 and the Ni K edges. The X-ray absorption near edge spectroscopy (XANES) spectrum analysis and the extraction of the atomic background were performed with the software ATHENA [58]. The fits of the extended X-ray absorption fine structure (EXAFS) oscillations were performed with the software ARTHEMIS [58]. **Fig. S1** and **Fig. S2** display the k^2 weighted EXAFS spectra and Fourier transforms of the $k^2\chi(k)$ EXAFS spectra measured at the Pt L_3, and at the Ni K edges, respectively. The first shell of interaction corresponds to the peaks with radial coordinates comprised between about 1 and 3 Å. **Table S1** shows structural parameters extracted from the Pt L_3 edge, such as N the number of Pt - Pt nearest-neighbours, R the A – B mean distance, and σ^2 the Debye-Waller factor.

Electron Microscopy

The synthesized electrocatalysts were deposited on a copper grid baring a Lacey carbon membrane for electron microscopy analyses. X-ray energy-dispersive spectroscopy (X-EDS) was performed using a LB FEI Titan 80-300 microscope equipped with a Cs probe corrector, and operated at 200 kV. A condenser aperture of 50 µm and a 128 mm camera length were used, yielding an electron probe with a convergence angle of 17 mrad. In order to get a high signal-to-noise ratio, a spot size 5 was used to obtain a beam current of 0.350 nA. The X-EDS spectra were recorded on individual nanoparticles by scanning the beam in a square region adjusted to the particle size using an acquisition time of 160 s. The quantitative analyses were performed on Pt L and Ni K lines using the *K*-factor provide by the FEI TIA software.

The high-resolution HAADF and the Spectrum-Imaging EELS analyses were recorded at CEA/PFNC Grenoble on a FEI Titan^3 Ultimate 80-300 microscope double Cs-corrected operated at 200 kV. The aberrations of the condenser lenses were corrected up to fourth-order using the Zemlin tableau to obtain a sub-Angstrom electron probe. A condenser aperture of 50 µm yielding an electron probe with a convergence angle of 20 mrad was used. The ADF collection angle ranged from 75-162 mrad and a 320 mm camera length on energy-filtered scanning transmission electron microscopy (EFSTEM) mode was used for EELS acquisitions, giving a collection semi-angle of 73 mrad. A Quantum-Gatan post column Imaging Filter (GIF) equipped with an ultra-fast shutter was used. To compensate for any sample drift during the analysis, a spatial drift correction was used every three line of the analysis. Every EEL spectrum was acquired using an acquisition time of 100 ms and an energy dispersion of 0.25 eV per channel. The matrix of spectra was de-noised using the standard principal component analysis and chemical maps were constructed analysing the Pt N_3 (518 eV) and Ni $L_{2,3}$ (855 eV) edges using a power-law background subtraction. Representative EEL spectra taken in the core or in the shell of the acid-treated Pt-Ni/C-AT nanoparticles are provided in **Fig. S3** and **Fig. S4**.

The metal nanoparticles were also examined with a Jeol 2010 TEM operated at 200 kV with a point to point resolution of 0.19 nm to build the particle size distribution of the catalysts, based on TEM images obtained at high magnifications (× 200 000). Since the synthesized Pt_xNi_{1-x}/C nanoparticles were irregularly shaped, the number of monolayers in the Pt-rich shell was estimated using the maximum Feret diameter of the outer-metal layer and of the inner core, after consideration of all possible diameters. The difference between the maximum Feret radius of the outer-metal layer and of the inner core was the shell thickness. For the reference spherical-shaped Pt/C electrocatalyst, a classical particle size distribution was established and the number-averaged was determined.

C. Electrochemical measurements

Electrochemical Measurements in Liquid Electrolyte

All the glassware accessories used in this study were cleaned by soaking in a H_2SO_4:H_2O_2 mixture overnight and thoroughly washing with ultrapure water. The 1 M H_2SO_4 solution used for acid-leaching and the 0.1 M H_2SO_4 electrolytic solution were prepared with Milli-Q water (Millipore, 18.2 MΩ cm, total organic compounds < 3 ppb) and H_2SO_4 96 wt % (Suprapur, Merck).

The measurements were conducted using an Autolab PGSTAT20 in a custom-made four-electrode electrochemical cell containing freshly prepared 0.1 M H_2SO_4 thermostated at T = 298 K. The counter-electrode was a large-area Pt foil and the reference electrode - a mercury sulphate electrode (MSE) $Hg|Hg_2SO_4|K_2SO_4$ (saturated, aqueous) - connected to the cell via a Luggin capillary. However, all electrode potentials reported were converted into the reversible hydrogen electrode (RHE) scale (E_{MSE} = 0.72 V *vs*. RHE). A Pt wire connected to the reference electrode was used to filter the high frequency electrical noise and to avoid disturbing the low frequency electrical measurements [59].

To prepare the working electrodes, an ink composed of 10 mg Pt/C from E-TeK, as-synthesized Pt-Ni/C or Pt-Ni/C-AT, 108 µL of 5 wt % Nafion® solution (Electrochem. Inc.), 40 µL of isopropanol and 4.8 mL (18.2 MΩ cm) of deionized water (MQ-grade, Millipore) was prepared according to a home-made procedure described in Ref. [33] After sonication for 15 minutes, 10 µL of the suspension was pipetted onto a glassy carbon disk, and sintered for 5 minutes at T = 383 K to ensure evaporation of the Nafion® solvents yielding a loading of *ca* 41.6 μg_{Pt} cm^{-2}. Prior to any electrochemical experiment, the working electrode was immersed into the deaerated electrolyte at E = 0.10 V *vs*. RHE (Ar >99.999 %, Messer). The real surface area was estimated using CO_{ad} stripping coulometry assuming that the electrooxidation of a CO_{ads} monolayer requires 420 µC per cm^2 of Pt. The CO saturation coverage was established by bubbling CO for 6 min and purging with Ar for 39 min, while keeping the electrode potential at E = 0.1 V *vs*. RHE. Two CO_{ad} stripping experiments were carried out before and after the electrocatalytic measurements to verify that no structural or chemical change occurred during the experiments: only slight variations (< 2 %) of the electrochemically active surface area (ECSA, cm^2_{Pt}) were monitored, and therefore the value determined before the ORR measurements was used. The ORR activity of the catalysts was measured in O_2-saturated 0.1 M H_2SO_4 solution (20 minutes of purging by oxygen > 99.99 %, Messer) by linearly sweeping the potential from 0.40 to 1.05 V at a potential sweep rate of 0.002 V s^{-1} and at a revolution rate of 1600 rpm. The ORR specific/mass activity was determined by normalizing the current measured at E = 0.90 V *vs*. RHE after correction from the oxygen diffusion in the solution to the real surface area/mass of deposited Pt.

Electrochemical Measurements in a PEM Fuel Cell (Solid Polymer Electrolyte)

The activity and the stability of the catalysts as PEMFC were tested in a single PEM fuel cell. For that purpose, membrane-electrodes assemblies (MEAs) were prepared using the decal method. First, inks with a concentration of 50 mg_C ml_{ink}^{-1} were prepared by putting together the catalysts (PtNi/C-AT or Pt/C 20wt.% for the cathode (E-TEK), Pt/C 40 wt.% for the anode (Tanaka Kikinzoku, ref number TEC10V40E), iso-propanol and an ionomer solution (Dupont® D2021). The ionomer to carbon weight ratio was 0.8 for all electrodes. 5 mm ZrO_2 grinding media were added to the ink, which were then homogenized overnight by roller milling. Inks were coated on 25 µm ETFE foil. After solvent evaporation, a Nafion XL membrane (Dupont®, 30 µm) was sandwiched between 5 cm^2 anode and cathode decals. This assembly was hot pressed at T = 428 K and 8 kN for 10 minutes. Similar cathode loadings of 0.16 mg_{Pt} cm^{-2} were achieved, calculated with the weight of the decals before and after hot pressing. The anode loadings were 0.4 mg_{Pt} cm^{-2}.

The MEAs were tested in 5 cm^2 active area single cell (Fuel Cell Technologies®). The conditioning procedures consisted of a one hour potential cycling (5 min at OCV, 10 min at U_{cell} = 0.85 and 45 min at U_{cell} = 0.65 V) repeated eight times, at T_{cell} = 333 K with fully humidified H_2/O_2 gases. Polarization curves were then recorded at T_{cell} = 353 K with fully humidified H_2 and O_2 gases. Total anode and cathode pressures were 150 kPa, fixed at the inlets of the cell. Stoichiometries of 2 and 9.5 were used for the anode and cathode reactants, respectively. Data points were recorded at 0.02; 0.05; 0.1; 0.2; 0.5; 1; 1.5 A cm^{-2} and finally the OCV (10 min $point^{-1}$ with data averaged for the last 10 sec). Impedance measurements were performed between 10^4 and 10 Hz at each current density for the measurement of high frequency resistances (HFR). Activities for the ORR at 0.90 V were deduced from HFR-corrected voltages versus H_2-crossover corrected currents semi-logarithmic plots.

Cyclic voltammograms (CV) were recorded between 0.070 V and 1 V at 0.020 V s^{-1}, T_{cell} = 353 K and 50 nccm fully humidified H_2 (anode) and 5 nccm dry N_2 (cathode) gases. H_2-crossover currents were measured at 0.4 V by averaging positive and negative going scans. The electrochemical active surface areas were deduced from the H_{upd} coulometry, assuming 210 µC cm^{-2} of Pt. Durability studies were performed by cycling the cathode electrode between 0.60 V and 1.05 V *vs*. RHE at a potential sweep rate of 0.050 V s^{-1}, using the same conditions than during CV measurements. Polarization curves and CV were also recorded after 1000 and 5000 potential cycles.

Results and discussion

A one-pot surfactant-free low-temperature synthesis was used to prepare carbon-supported hollow Pt_xNi_{1-x}/C nanoparticles. In a typical synthesis, Pt and Ni precursor solutions were mixed with Vulcan XC72R®, ethanol and de-ionized water. The metal precursors were then reduced by continuous addition of sodium borohydride under vigorous magnetic stirring. The resulting mixture was filtered, thoroughly washed by de-ionized water and dried at T = 383 K to yield Pt-Ni/C nanocrystallites (**Fig 1a and Fig. 1c**). A fraction of this powder was then acid-treated for 12 h in a stirred 1 M H_2SO_4 solution at T = 293 K. This sample is referred to as the Pt-Ni/C-AT electrocatalyst (**Fig 1b** and **Fig. 1d-g**).

The HAADF-STEM images of **Fig. 1** show that individual hollow nanoparticles are formed by metal nanocrystallites *ca*. 3 nm in size, interconnected by grain boundaries, and arranged into a closed metal shell. **Fig 1e** and **Fig. 1g** display fast Fourier Transform of **Fig 1d** and **Fig. 1f**, giving information on the lattice parameter and crystallography of the Pt-Ni/C-AT nanoparticles: the multiple spots arranged on concentric rings (assigned to diffraction from {111}, {200}, and {220} planes) indicate that the metal hollow nanoparticles are polycristalline. The average d spacing of 0.22-0.23 nm measured in **Fig. 1d** and **Fig. 1f** corresponds to the (111) lattice planes in a face-centred cubic (fcc) Pt phase. Comparing **Fig 1a** and **Fig. 1b** shows that the acid-treatment did not modify the hollow nanostructure.

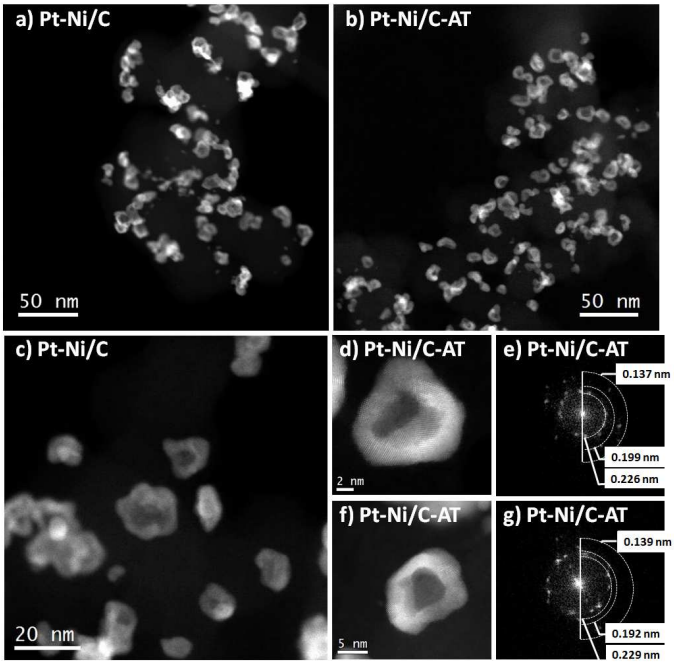

Fig. 1. Aberration-corrected HAADF-STEM images and digital diffraction pattern (DDP; insets) of the as-synthesized Pt-Ni/C (a, c) and the Pt-Ni/C-AT nanoparticles (b, d, e, f, g). Marked in DDPs are reflections characteristic of the cubic phase in the [hkl] zone axis.

The X-ray diffraction patterns of **Fig. 2** confirm the fcc structure of the synthesized and reference electrocatalysts. Similar broadening of the diffraction peaks suggests similar crystallite size for all the samples (according to the Scherrer equation). The positive shift of the X-ray reflections towards larger 2θ angles indicates that the lattice parameter is contracted by *ca*. 1.2 % in average in the synthesized

electrocatalyst *vs*. solid Pt/C nanocrystallites of the same size. The lattice parameter contraction remained constant upon acid treatment (see inset).

Table 1. Structural and chemical parameters of the as-synthesized and acid-treated Pt_xNi_{1-x}/C nanoparticles extracted from STEM images, X-ray diffractograms, X-EDS and X-ray absorption spectra.

	Pt-Ni/C	Pt-Ni/C-AT	Pt/C
Pt:Ni in precursor solution	1:1	1:1	-
At comp. from X-EDS	$Pt_{69}Ni_{31}$	$Pt_{89}Ni_{11}$	Pt_{100}
At comp. from XANES	$Pt_{66}Ni_{33}$	$Pt_{89}Ni_{11}$	-
$\overline{d}_N$ (nm) from HAADF-STEM	13.2 ± 3.8	13.7 ± 2.5	2.8 ± 0.1
$\overline{d}_{XRD}$ (nm) from XRD	1.72 ± 0.15	3.02 ± 0.15	2.24 ± 0.15
Interatomic distance (nm)	0.2747 ± 0.0003	0.2745 ± 0.0003	0.2779 ± 0.0003
Pt-shell thickness (nm) from STEM	-	3.6 ± 0.8	-

X-EDS spectra performed on a group of Pt_xNi_{1-x}/C nanoparticles revealed a global Ni content of *ca*. 31 ± 12 % in the as-synthesized Pt-Ni/C electrocatalyst (**Table 1**). The Ni content decreased to 11 ± 8 at. % after acid treatment (**Fig. 3**).

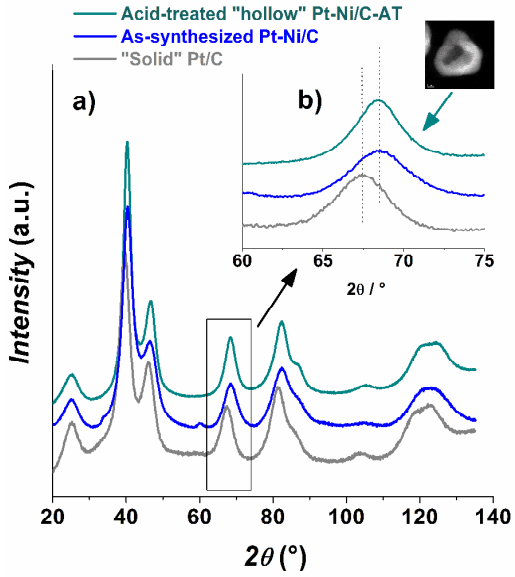

Fig. 2. X-ray diffraction patterns of (a) of the Pt-Ni/C, the Pt-Ni/C-AT, and the reference Pt/C electrocatalysts, and (b) zoom in the 60 < 2θ < 75° region showing the lattice contraction in the hollow Pt-Ni/C and Pt-Ni/C-AT nanoparticles relative to Pt/C. For interpretation of the references to colour in this Fig. legend, the reader is referred to the web version of this article.

The efficiency of the acid-leaching procedure was confirmed by XANES experiments. **Fig. 4a** and **Fig. 4b** present normalized XANES spectra collected at the Pt L_3 and the Ni K edges on the Pt-Ni/C and Pt-Ni/C-AT electrocatalysts, respectively. The Pt L_3 features remained nearly unchanged after the acid treatment, providing evidence that the electronic structure of the Pt atoms was not modified during this procedure. Conversely, the XANES spectra recorded at the Ni K edge indicate the presence of Ni oxides in the as-synthesized Pt-Ni/C electrocatalyst, while after acid treatment only features of metallic Ni were found. This suggests that Ni nanoparticles not covered with Pt were dissolved during the acid leaching procedure. The Pt:Ni atomic composition in the electrocatalysts was determined from the X-ray absorption jump intensities recorded at the Pt L_3 and at the Ni K edges in transmission mode, following the approach of Durst *et al*. [60]. The Ni atomic content estimated by XANES dropped from 33 to 11 % upon the acid treatment, in agreement with the X-EDS analysis (**Table 1**).

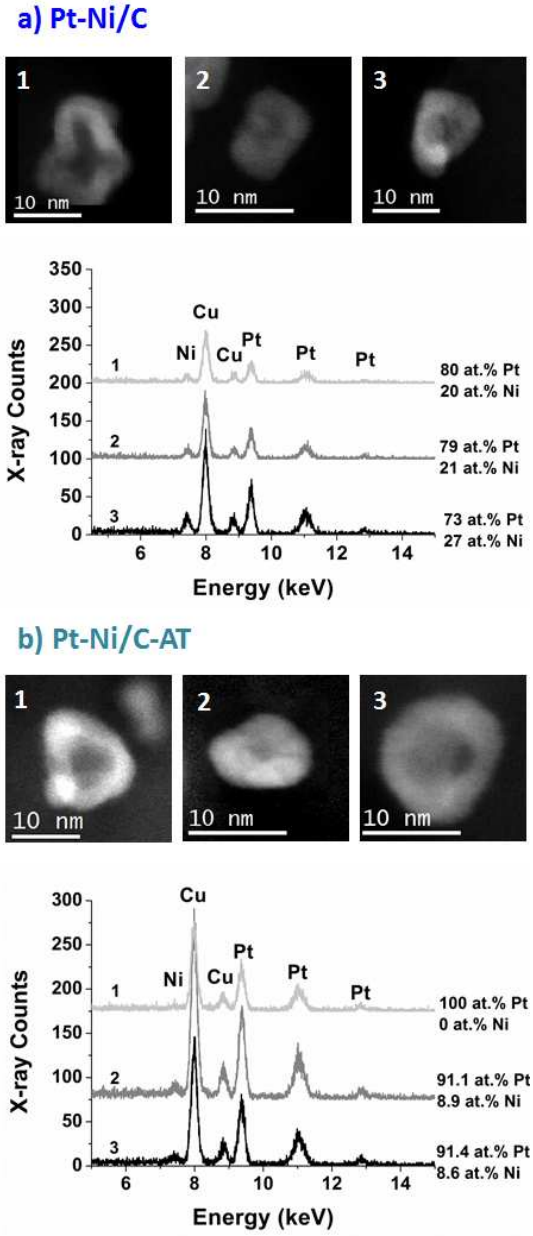

Fig. 3. Aberration-corrected HAADF-STEM images and X-EDS spectra measured on the as-synthesized Pt-Ni/C and the Pt-Ni/C-AT nanoparticles. The particle-averaged at % of Pt and Ni in individual nanoparticles are indicated on the right-hand side of the X-EDS spectra. The copper signal arises from the copper grid where the catalyst is deposited for TEM measurements.

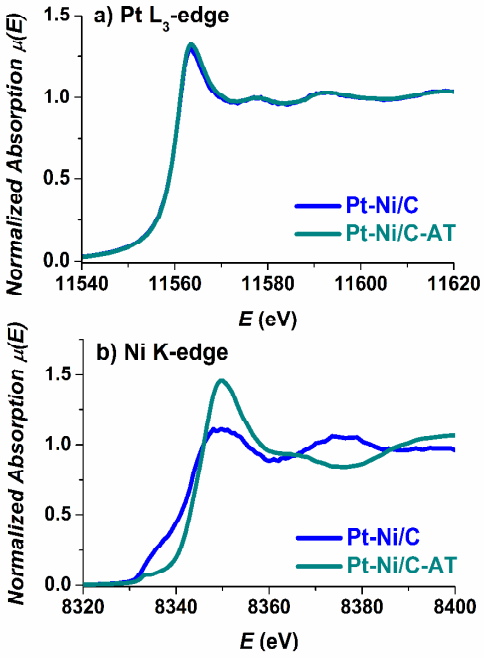

Fig. 4. Normalized XANES signals measured in transmission mode at the (a) Pt L_3 edge and (b) Ni K edge for the Pt-Ni/C (in blue) and the Pt-Ni/C-AT (in dark cyan) samples. For interpretation of the references to colour in this Fig. legend, the reader is referred to the web version of this article.

The EXAFS spectra measured on the as-synthesized and acid-treated electrocatalysts are provided in **Fig. S1 and Fig. S2.** At the Ni K edge, typical features of Ni-O bonds were observed for the Pt-Ni/C catalyst. At the Pt L_3 edge, the best fit of the EXAFS spectra was obtained by considering Pt-Pt, and no Pt-Ni bond. This can be understood by considering a smaller number of Pt-Ni bonds (*e.g.* those present at the core | shell interface) compared to that of Ni-Ni or Pt-Pt bonds (present in the core and shell, respectively). The same reasoning holds true for the hollow Pt-Ni/C-AT electrocatalyst. Interestingly, for this material, the total coordination number - N_{Pt} = 7.5, see **Table S1** - is well below that expected for 3-4 nm-sized crystallites ($N_{Pt} \approx$ 10 - 10.5). This can be rationalized by considering the contribution of both the outer-surface and the inner-surface atoms (*e.g.* those in "contact" with the central cavity) to the apparent decrease of N_{Pt}. Finally, the Pt-Pt bond distance estimated from the fit of the EXAFS spectra is contracted by 1.8 % for the hollow *vs*. the reference Pt/C nanocatalysts, in agreement with XRD estimates (**Table S1**).

Additional insights into the chemical distribution of Pt and Ni elements were obtained from electron energy-loss spectroscopy in spectrum imaging mode (EELS-SI, see **Fig. 5**). EELS-SI maps of the Pt-Ni/C-AT electrocatalyst revealed the presence of: (i) hollow Pt-Ni/C or Pt/C nanoparticles, and (ii) core-shell nanoparticles characterized by a Ni-rich core surrounded by a 3.6 ± 0.8 nm thick Pt-rich shell (in average, *i.e.* 16 ± 4 monolayers of Pt, assuming a (111) lattice spacing of 0.23 nm). The fraction of hollow and core-shell nanoparticles was determined using HAADF-STEM images. Out of 104 analysed nanoparticles, 71 were found to be hollow (68 %) and 33 (32 %) were solid nanoparticles. The atomic composition of the three different nanostructures was determined using X-EDS analyses over individual nanoparticles: 50 % of the hollow nanoparticles were found to be pure Pt, and the other 50 % had Ni content below 10 at. %. The solid nanoparticles featured core-shell structure and Ni content comprised between 20 and 25 at. %.

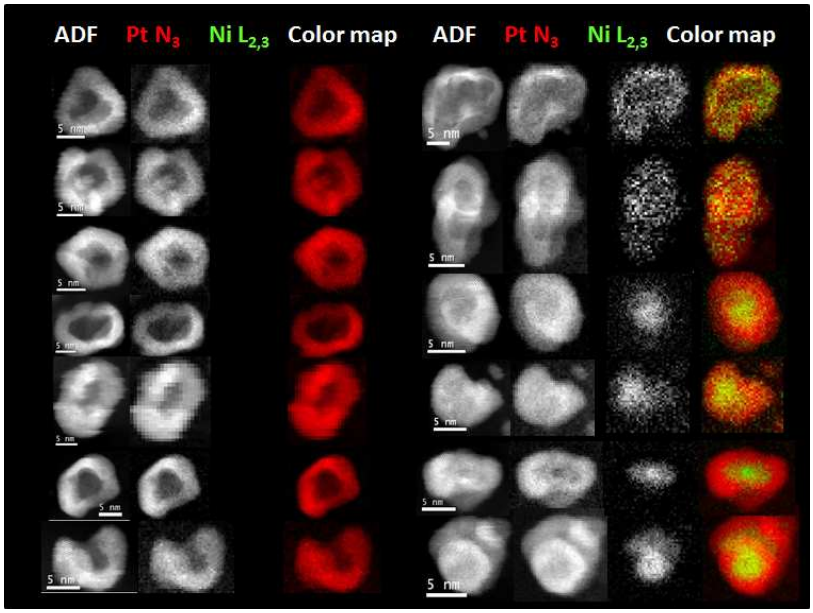

Fig. 5. ADF images and chemical maps of individual Pt-Ni/C-AT nanoparticles. The spectroscopic maps provide direct evidence of the presence of two types of nanostructures: (i) hollow Pt-Ni/C or Pt/C nanoparticles, and (ii) core-shell nanoparticles characterized by a Ni-rich core surrounded by an average 3.6 ± 0.8 nm thick

Pt-rich shell. In the colour maps, the Pt N_3 signal is shown in red, and the Ni $L_{2,3}$ signal is shown in green. Representative EEL spectra measured in the core/shell areas of hollow and core-shell Pt-Ni/C-AT nanoparticles are provided in Fig. S3 and Fig. S4, respectively. For interpretation of the references to colour in this Fig. legend, the reader is referred to the web version of this article.

The adsorption/desorption of underpotentially-deposited hydrogen (H_{upd}) and the electrooxidation of a CO_{ad} monolayer were used to probe the surface composition and the fine nanostructure of the hollow metal nanoparticles (**Fig. 6**). The typical Pt-like underpotentially-deposited hydrogen (H_{upd}) features confirm the conclusions derived from EELS-SI: the surface and near-surface regions of the Pt-Ni/C-AT nanoparticles are almost pure Pt. In CO_{ad} stripping experiments, similarities but also differences were noted. On the one hand, the identical position of the high potential CO_{ad} electrooxidation peak measured on solid and hollow nanoparticles (E = 0.82 V *vs.* RHE) suggests identical Pt-shell thickness/crystallite size for both samples (the position of the high potential peak in CO_{ad} stripping voltammograms scales inversely with the mean crystallite size, see Refs. [39, 61]), confirming the assertions derived from XRD measurements. On the other hand, the "double-peak" at E = 0.72 and 0.76 V *vs.* RHE, which is assigned to CO_{ads} electrooxidation peak on defective crystallites, [61, 62] is present on the hollow Pt-Ni/C-AT nanoparticles, and not on the reference Pt/C electrocatalyst. This is not surprising since the hollow nanoparticles feature grain boundaries in the Pt-rich shell itself (see **Fig. 1d**) but also are connected to other nanoparticles via inter-grain boundaries (in other words, some of the hollow nanoparticles are agglomerated, see **Fig. 1b**).

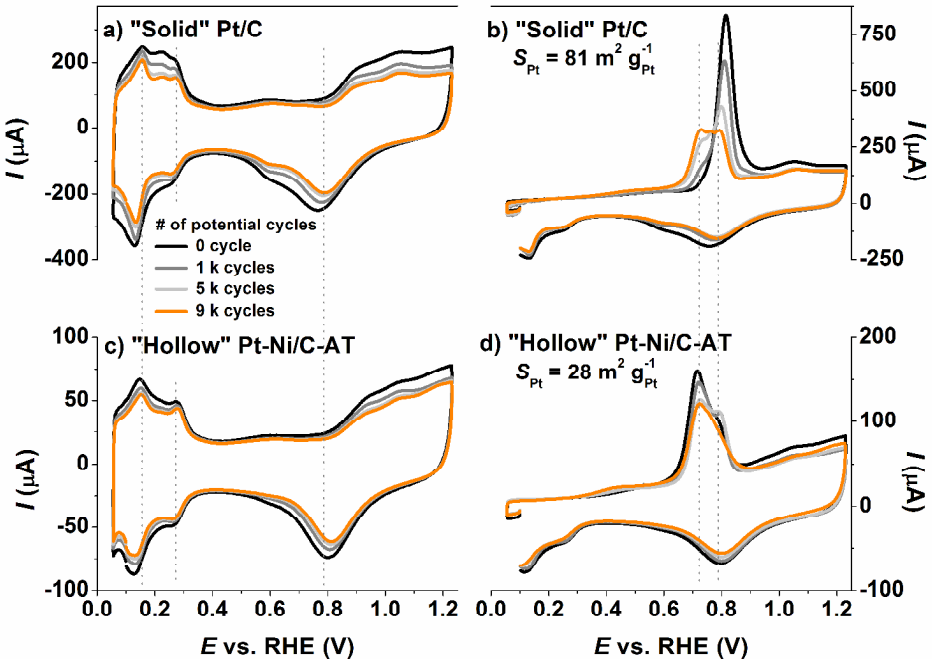

Fig. 6. Accelerated stress tests performed on the hollow Pt-Ni/C-AT, and on the reference Pt/C electrocatalysts (9 k potential cycles between 0.60 and 1.05 V *vs.* RHE). (a, c) Base and (b, d) CO_{ad} stripping voltammograms. Electrolyte: 0.1 M H_2SO_4; v = 0.020 V s^{-1}; T = 298 ± 1 K, no rotation, catalyst loading 41.2 μg$_{Pt}$ geometrical cm^{-2}.

Accelerated stress tests (ASTs) were performed to investigate the stability of the hollow Pt-Ni/C-AT and the reference solid Pt/C nanoparticles in model and real PEMFC operating conditions (**Fig. 6**). The aging procedure consisted of 9,000 (9 k) potential cycles between 0.60 V *vs.* RHE and 1.05 V *vs.* RHE at a sweep rate v = 0.05 V s^{-1} in 0.1 M H_2SO_4 and T = 298 K (liquid electrolyte), or 5,000 potential cycles in solid polymer electrolyte and T = 353 K (PEMFC single cell testing) at the same potential sweep rate. Such experimental conditions simulate the typical potential range experienced by a cathode material during PEMFC operation (*i.e.* at high and low current density, during idling and open circuit conditions) [8, 30, 63]. The changes in ECSA or in specific surface area per mass (S_{Pt}, m^2 g$^{-1}_{Pt}$) were monitored via CO_{ad} stripping coulometry or H_{upd} desorption coulometry experiments in liquid or solid electrolyte, respectively. **Fig. 6** highlights some of the trends observed on the hollow and the reference solid electrocatalysts during the AST. On the solid Pt/C nanoparticles, the changes of the number/intensity of H_{upd} peaks, the positive shift of the Pt-oxide reduction peak and the negative shift of the main CO_{ad} stripping peak are clear markers of Pt nanocrystallite growth [61, 62]. The increased electrical charge under the CO_{ad} electrooxidation pre-peak suggests the formation of Pt/C agglomerates [61]. On the contrary, for the hollow Pt-Ni/C-AT nanoparticles, the H_{upd} adsorption/desorption, the Pt-oxide reduction and the CO_{ad} stripping features remain largely unchanged upon the AST. Since the surface and near-surface layers of both hollow and core-shell nanostructures are Pt-rich

(**Fig. 5**), the better resistance of the hollow nanoparticles to Pt dissolution should be ascribed to their particular nanostructure. In particular, it is well-established that catalysts featuring contracted lattice parameter possess weakened oxophilicity relative to solid Pt/C nanoparticles. In consequence, since Pt-O is an intermediate in the Pt dissolution mechanism, [64-66] it is not surprising that the hollow Pt-Ni/C-AT nanoparticles are more resistant to the electrochemical/chemical dissolution than the solid Pt/C nanoparticles. In addition, due to their larger particle size, the hollow nanoparticles feature a decreased surface fraction of low-coordination sites or defects, where Pt dissolution is known to initiate [65, 66]. These characteristics make hollow Pt-Ni/C-AT nanoparticles particularly suitable to sustain long-term performance at a PEMFC cathode.

The catalytic activity of the synthesized and reference samples were determined at E = 0.90 V *vs.* RHE ($SA_{0.90}$ and $MA_{0.90}$, respectively) in liquid electrolyte at T = 298 K and during PEMFC operation at T = 353 K. The measured ORR current was normalized with respect to the geometrical surface area of the electrode (**Fig. 7a and Fig. 7b**), the Pt loading of the electrode (mass activity, **Fig. 7c**, **Fig. 7d, Fig. 8e and Fig. 8f**) or the Pt electrochemically active surface area (specific activity, **Fig. 8c** and **Fig. 8d**). Whatever the normalization and the electrolyte, electrodes composed of hollow Pt-Ni/C-AT nanocrystallites showed improved catalytic performance over solid Pt/C. At E = 0.90 V *vs.* RHE, the synthesized hollow Pt-Ni/C-AT nanoparticles achieved 4-fold and 5-fold enhancement of the ORR specific activity over Pt/C nanocrystallites of the same size in liquid electrolyte and solid polymer electrolyte, respectively (**Fig. 8**). These enhancement factors are comparable to those obtained with dealloyed Pt-M/C nanomaterials [4, 67] or nanostructured Pt-M thin films [3]. However, and contrary to these reference materials, the hollow nanoparticles maintain this high level of performance on the long-term in model but also in real PEMFC operating conditions.

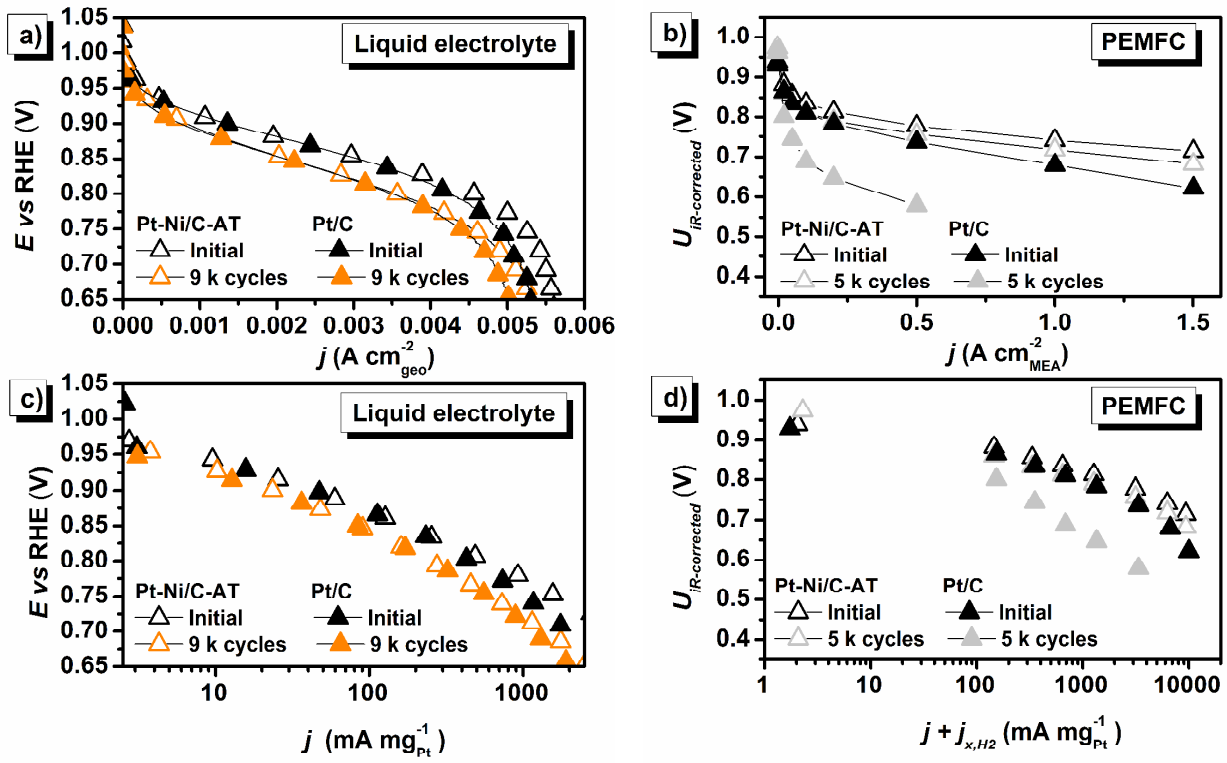

Fig. 7. (a) Linear sweep voltammograms recorded at ω = 1600 rpm on the hollow Pt-Ni/C-AT and on the reference solid Pt/C nanoparticles (b) and corresponding polarization curves measured on a 5 cm^2 single PEMFC; Tafel plots of (c) the mass transport-corrected kinetic current obtained from the steady-state *I–E* curves in liquid electrolyte and (d) the kinetic current obtained from the polarization curves after correction from Ohmic resistance measured by impedance spectroscopy. In the PEMFC tests, the cathodes were based on the hollow Pt-Ni/C-AT nanoparticles or the reference Pt/C electrocatalysts, loaded both at 0.16 mg_{Pt} cm^{-2}_{geo}. A Pt/C 40 wt. % catalyst was used at the anode, loaded at 0.40 mg_{Pt} cm^{-2}_{geo}. The PEM was a Nafion® XL, 30 µm. Ionomer Nafion® D2021 (20 wt % of ionomer, equivalent weight 1000 g mol^{-1}). T_{cell} = 353 K. The MEA operated with fully humidified gases at $P_{H2/O2}$ = 100 kPa with stoichiometric flows s = 2/9.5 for I > 0.5 A.

The better catalytic activity of the hollow Pt-Ni/C-AT nanoparticles is believed to arise from the vacancies-induced contraction of the Pt lattice parameter evidenced by X-ray diffraction and Synchrotron X-ray absorption spectroscopy measurements. The recent density functional theory calculations of Callejas-Tovar *et al.* [68] strongly support this theory: the authors demonstrated that an increased amount of vacancies in the subsurface layers decreases the binding energy of OH, and enhances the ORR activity of pure Pt electrocatalysts. It could be argued that Ni atoms contained in

the core-shell nanoparticles also play a role *via* ligand or strain effect. However, the EELS-SI chemical maps (**Fig. 5**) showed that the Ni–rich cores are covered by 16 ± 4 atomic layers of Pt in average. In consequence, a direct influence of residual Ni atoms on Pt surface reactivity is very unlikely (it is well-established that the modifications of the geometric and the electronic structure of Pt induced by direct interaction with a non-noble transition metal element vanish after a few atomic layers [11, 69, 70]). The low specific surface area of hollow Pt-rich nanocrystallites (S_{Pt} = 28 m^2 g_{Pt}^{-1}) is currently a disadvantage of the synthesized electrocatalysts. In spite of this, superior mass activity values were measured relative to a reference Pt/C electrocatalyst (S_{Pt} = 81 m^2 g_{Pt}^{-1}) at identical Pt loading in the electrode. Consequently, there is room for improvements, and preliminary results have revealed constant $SA_{0.90}$ but doubled S_{Pt} and $MA_{0.90}$ values when different initial Pt:Ni stoichiometry is used to synthesize the hollow Pt-Ni/C-AT nanocrystallites.

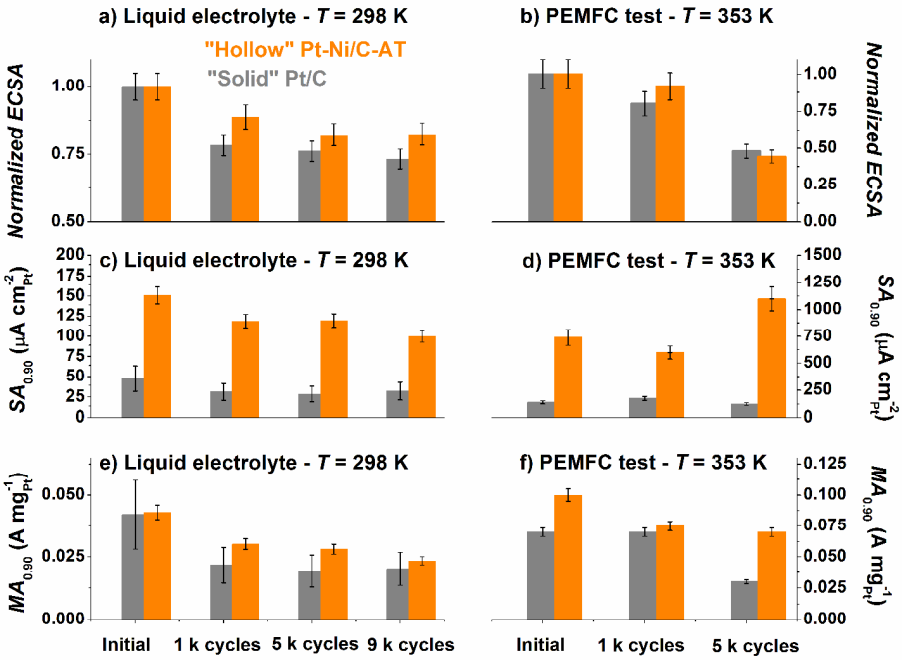

Fig. 8. Time evolution of (a, b) the Pt ECSA, (c, d) the ORR specific activity and (e, f) the ORR mass activity during an accelerated stress test consisting of potential cycles between 0.60 and 1.05 V *vs.* RHE. The Pt specific surface area was measured via CO_{ad} stripping coulometry at a potential sweep rate of 0.020 V s^{-1} in 0.1 M H_2SO_4 and T = 298 ± 1 K in (a) and via the H_{upd} desorption coulometry at a potential sweep rate of 0.020 V s^{-1} in PEMFC and T = 353 ± 1 K in (b). The activity for the ORR was evaluated from mass transport-corrected kinetic currents measured at (c, e) E = 0.90 V *vs* RHE in O_2-saturated 0.1 M H_2SO_4; potential sweep rate 0.002 V s^{-1}; positive-going potential sweep from 0.40 to 1.10 V *vs.* RHE; T = 298 ± 1 K, and (d, f) from iR-corrected voltages versus H_2-crossover corrected currents semi-logarithmic plots. The currents are normalized to the real surface area estimated by CO_{ad} stripping or H_{upd} desorption coulometry in (c, e) or (d, f) respectively. Each value is the average of at least three measurements. The error bars represent (a, b, d) the estimated incertitude associated with Pt ECSA determination, (c, e) the standard deviation of the measurements.

Conclusions

In conclusion, hollow carbon-supported Pt_xNi_{1-x}/C nanoparticles with low Ni content (11 at. %) have been successfully synthesized *via* a method involving the galvanic replacement of Ni atoms by Pt atoms, and the nanoscale Kirkendall effect. EELS-SI, and X-EDS measurements indicated that hollow Pt-rich nanoparticles represent the predominant nanostructure in the catalyst, and XRD measurements revealed a contraction of the Pt lattice by *ca.* 1.2 % in hollow relative to solid Pt nanoparticles. The hollow Pt-Ni/C-AT nanoparticles show improved and sustainable ORR specific activity in liquid electrolyte and in PEMFC operating conditions. Further optimization of the hollow nanostructure by easily-controllable parameters, such as the Pt:Ni stoichiometry in the metal salt precursor solution, is currently being undertaken to increase the Pt specific surface area and the ORR mass activity.

Acknowledgements

This work was performed within the framework of the Centre of Excellence of Multifunctional Architectured Materials "CEMAM". The authors acknowledge financial support from University Grenoble-Alpes through the AGIR program (grant # LL1492017G), the French national Research Agency (grant # ANR-14-CE05-0003-01) and thank Dr. Jean-Louis Hazemann, Dr. Olivier Proux and all the members of the FAME team for their kind help to the realization of the XAS measurements on the beamline BM30B of the European Synchrotron Radiation Facility (ESRF). These measurements were performed in the frame of the ESRF projects 30-02 1054 and 30-02 1058. M.L.H. thanks the MECD Spanish Ministry (ref. EX2010-1135) for funding part of his post-doctoral stay at CEA-INAC. MC thanks the French IUF for its support.

Notes and references

a Univ. Grenoble Alpes, LEPMI, F-38000 Grenoble, France
b CNRS, LEPMI, F-38000 Grenoble, France
c Univ. Grenoble Alpes, INAC-SP2M, LEMMA, F-38000 Grenoble, France
d Institute of Technical Electrochemistry, Technische Universität München, Lichtenbergstrasse 4, D-85748, Garching, Germany

e CEA, LITEN, Département des Technologies de l'Hydrogène, Laboratoire des Composants PEM, 17 rue des Martyrs, 38054 Grenoble, France
f Member of the French University Institute, IUF, Paris, France

† Here "solid" means: "having the interior completely filled up, free from cavities, i.e. nanocrystallites that contain no holes".

Electronic Supplementary Information (ESI) available: [Fig. S1. k^2 weighted EXAFS spectra measured at the (A) Pt L_3 and (B) the Ni K edges on the Pt-Ni/C (blue) and the Pt-Ni/C-AT (dark cyan lines) catalysts. – Fig. S2. Fourier transform (FT) magnitudes of the $k^2\chi$ (k) EXAFS spectra measured at the a) Pt L_3 and b) Ni K edges for the Pt-Ni/C (blue) and the Pt-Ni/C-AT (dark cyan lines) catalysts. – Fig. S3. (a) Representative EEL spectra measured on a hollow Pt-Ni/C-AT nanoparticle. The brutto signal is displayed in blue, the background subtraction using a power law function is shown in red and the background-subtracted signal is displayed in green. The inset displays the ADF image of the analyzed Pt-Ni/C-AT nanoparticle. (b) Pt N_3 and Ni $L_{2,3}$ elemental mapping and (c) Background subtracted EEL spectra extracted from the sites marked in black (nanoparticle shell) and red (nanoparticle core) rectangles. – Fig. S4. (a) Representative EEL spectra measured on a core-shell Pt-Ni/C-AT nanoparticle. The brutto signal is displayed in blue, the background subtraction using a power law function is shown in red and the background-subtracted signal is displayed in green. The inset displays the ADF image of the analyzed Pt-Ni/C-AT nanoparticle. (b) Pt N_3 and Ni $L_{2,3}$ elemental mapping and (c) Background subtracted EEL spectra extracted from the sites marked in black (nanoparticle shell) and red (nanoparticle core) rectangles. –Table S1. Structural parameters obtained from the best fits of the FTs for the Pt-Ni/C and the Pt-Ni/C-AT electrocatalysts (Pt edge). σ^2 is the mean square radial disorder, and the *R*-factor indicates the quality of the fit from which the data reported in this table are extracted.]. See DOI: 10.1039/b000000x/

1. H. A. Gasteiger and N. M. Markovic, *Science*, 2009, **324**, 48-49.
2. F. T. Wagner, B. Lakshmanan and M. F. Mathias, *J. Phys. Chem. Lett.*, 2010, **1**, 2204-2219.
3. M. K. Debe, *Nature*, 2012, **486**, 43-51.
4. M. Oezaslan, F. Hasché and P. Strasser, *J. Phys. Chem. Lett.*, 2013, **4**, 3273-3291.
5. F. Maillard, S. Pronkin and E. R. Savinova, in *Fuel Cell Catalysis: a Surface Science Approach*, ed. M. T. M. Koper, John Wiley & Sons, Inc., New York, 2009, pp. 507-566.
6. C. Wang, D. van der Vliet, K.-C. Chang, H. You, D. Strmcnik, J. A. Schlueter, N. M. Markovic and V. R. Stamenkovic, *J. Phys. Chem. C*, 2009, **113**, 19365-19368.
7. Y. Shao-Horn, W. Sheng, S. Chen, P. Ferreira, E. Holby and D. Morgan, *Topics Catal.*, 2007, **46**, 285-305.
8. M. F. Mathias, R. Makharia, H. Gasteiger, J. J. Conley, T. J. Fuller, G. J. Gittleman, S. S. Kocha, D. P. Miller, C. K. Mittelsteadt, T. Xie, S. G. Yan and P. T. Yu, *Interface*, 2005, **14**, 24-35.
9. F. T. Wagner, S. G. Yan and P. T. Yu, in *Handbook of Fuel Cells*, eds. W. Vielstich, H. Yokokawa and H. Gasteiger, John Wiley & Sons, Ltd, 2009, pp. 250-263.
10. V. R. Stamenkovic, B. S. Mun, M. Arenz, K. J. J. Mayrhofer, C. A. Lucas, G. F. Wang, P. N. Ross and N. M. Markovic, *Nature Mater.*, 2007, **6**, 241-247.
11. P. Strasser, S. Koh, T. Anniyev, J. Greeley, K. More, C. Yu, Z. Liu, S. Kaya, D. Nordlund, H. Ogasawara, M. F. Toney and A. Nilsson, *Nat. Chem.*, 2010, **2**, 454-460.
12. S. J. Bae, S. J. Yoo, Y. Lim, S. Kim, Y. Lim, J. Choi, K. S. Nahm, S. J. Hwang, T. H. Lim, S. K. Kim and P. Kim, *J. Mater. Chem.*, 2012, **22**, 8820.
13. J. Snyder, I. McCue, K. Livi and J. Erlebacher, *J. Am. Chem. Soc.*, 2012, **134**, 8633-8645.
14. L. Gan, M. Heggen, S. Rudi and P. Strasser, *Nano Lett.*, 2012, **12**, 5423−5430.
15. C. Cui, L. Gan, M. Heggen, S. Rudi and P. Strasser, *Nature Mater.*, 2013, **12**, 765–771.
16. D. L. Wang, H. L. L. Xin, R. Hovden, H. S. Wang, Y. C. Yu, D. A. Muller, F. J. DiSalvo and H. D. Abruna, *Nature Mater.*, 2013, **12**, 81-87.
17. C. Chen, Y. Kang, Z. Huo, Z. Zhu, W. Huang, H. L. Xin, J. D. Snyder, D. Li, J. A. Herron, M. Mavrikakis, M. Chi, K. L. More, Y. Li, N. M. Markovic, G. A. Somorjai, P. Yang and V. R. Stamenkovic, *Science*, 2014, **343**, 1339-1343.
18. J. Zhang, M. B. Vukmirovic, Y. Xu, M. Mavrikakis and R. R. Adzic, *Angew. Chem. Int. Ed.*, 2005, **44**, 2132-2135.
19. R. R. Adzic, J. Zhang, K. Sasaki, M. B. Vukmirovic, M. Shao, J. X. Wang, A. U. Nilekar, M. Mavrikakis, J. A. Valerio and F. Uribe, *Topics Catal.*, 2007, **46**, 249-262.
20. L. Gan, C. Cui, S. Rudi and P. Strasser, *Topics Catal.*, 2014, **57**, 236-244.
21. C. Cui, L. Gan, M. Neumann, M. Heggen, B. Roldan Cuenya and P. Strasser, *J. Am. Chem. Soc.*, 2014, **136**, 4813-4816.
22. B. Hammer and J. K. Nørskov, *Surf. Sci.*, 1995, **343**, 211-220.
23. K. Matsuzawa, T. Fukushima and M. Inaba, *Electrocatalysis*, 2010, **1**, 169-177.
24. L. Gan, M. Heggen, R. O'Malley, B. Theobald and P. Strasser, *Nano Lett.*, 2013, **13**, 1131-1138.
25. C. Cui, M. Ahmadi, F. Behafarid, L. Gan, M. Neumann, M. Heggen, B. R. Cuenya and P. Strasser, *Faraday Discuss.*, 2013, **162**, 91-112.
26. Y. Ma and P. B. Balbuena, *J. Chem. Theory Comput.*, 2008, **4**, 1991-1995.
27. Y. Ma and P. B. Balbuena, *J. Phys. Chem. C*, 2008, **112**, 14520-14528.
28. Y. G. Ma and P. B. Balbuena, *Surf. Sci.*, 2008, **602**, 107-113.
29. Y. Ma and P. B. Balbuena, *Surf. Sci.*, 2009, **603**, 349-353.
30. S. Chen, H. A. Gasteiger, K. Hayakawa, T. Tada and Y. Shao-Horn, *J. Electrochem. Soc.*, 2010, **157**, A82-A97.
31. F. Maillard, L. Dubau, J. Durst, M. Chatenet, J. André and E. Rossinot, *Electrochem. Commun.*, 2010, **12**, 1161-1164.
32. L. Dubau, F. Maillard, M. Chatenet, L. Guétaz, J. André and E. Rossinot, *J. Electrochem. Soc.*, 2010, **157**, B1887-B1895.
33. L. Dubau, F. Maillard, M. Chatenet, L. Guétaz, J. André and E. Rossinot, *Electrochim. Acta*, 2011, **56**, 10658-10667.
34. R. Callejas-Tovar, W. Liao, H. Mera and P. B. Balbuena, *J. Phys. Chem. C*, 2011, **115**, 23768-23777.
35. C. Wang, M. Chi, G. Wang, D. van der Vliet, D. Li, K. More, H.-H. Wang, J. A. Schlueter, N. M. Markovic and V. R. Stamenkovic, *Adv. Funct. Mater.*, 2011, **21**, 147-152.
36. D. A. Cantane, F. E. R. Oliveira, S. F. Santos and F. H. B. Lima, *Appl. Catal. B.*, 2013, **136**, 351-360.
37. J. Durst, M. Chatenet and F. Maillard, *Phys. Chem. Chem. Phys.*, 2012, **14**, 13000-13009.

38. L. Dubau, M. Lopez-Haro, L. Castanheira, J. Durst, M. Chatenet, P. Bayle-Guillemaud, L. Guétaz, N. Caqué, E. Rossinot and F. Maillard, *Appl. Catal. B*, 2013, **142-143**, 801-808.
39. L. Dubau, F. Maillard, M. Chatenet, J. André and E. Rossinot, *Electrochim. Acta*, 2010, **56**, 776-783.
40. M. Oezaslan, M. Heggen and P. Strasser, *J. Am. Chem. Soc.*, 2012, **134**, 514-524.
41. A. Greszler, T. Moylan and H. A. Gasteiger, in *Handbook of Fuel Cells: Fundamentals, Technology, and Applications*, eds. W. Vielstich, H. A. Gasteiger and H. Yokokawa, John Wiley & Sons, Chichester, 2009, pp. 728-748.
42. M. Chatenet, L. Guétaz and F. Maillard, in *Handbook of Fuel Cells*, eds. W. Vielstich, H. A. Gasteiger and H. Yokokawa, John Wiley & Sons, Inc., New York, 2009, pp. 844-860.
43. A. Bonakdarpour, R. Lobel, R. T. Atanasoski, G. D. Vernstrom, A. K. Schmoeckel, M. K. Debe and J. R. Dahn, *J. Electrochem. Soc.*, 2006, **153**, A1835-A1846.
44. E. O. Kirkendall, *Trans. AIME*, 1942, **147**, 104-109.
45. A. D. Smigelskas and E. O. Kirkendall, *Trans. AIME*, 1947, **171**, 130-142.
46. Y. D. Yin, R. M. Rioux, C. K. Erdonmez, S. Hughes, G. A. Somorjai and A. P. Alivisatos, *Science*, 2004, **304**, 711-714.
47. H. J. Fan, U. Gosele and M. Zacharias, *Small*, 2007, **3**, 1660-1671.
48. E. González, J. Arbiol and V. F. Puntes, *Science*, 2011, **334**, 1377-1380.
49. P. B. Balbuena, R. Callejas-Tovar, P. Hirunsit, J. M. Martínez De La Hoz, Y. Ma and G. E. Ramírez-Caballero, *Topics Catal.*, 2012, **55**, 322-325.
50. M. Lopez-Haro, L. Dubau, L. Guétaz, P. Bayle-Guillemaud, M. Chatenet, J. André, N. Caqué, E. Rossinot and F. Maillard, *Appl. Catal. B*, 2014, **152-153**, 300-308.
51. J. X. Wang, C. Ma, Y. Choi, D. Su, Y. Zhu, P. Liu, R. Si, M. B. Vukmirovic, Y. Zhang and R. R. Adzic, *J. Am. Chem. Soc.*, 2011, **133**, 13551-13557.
52. Y. Zhang, C. Ma, Y. M. Zhu, R. Si, Y. Cai, J. X. Wang and R. R. Adzic, *Catal. Today*, 2013, **202**, 50-54.
53. Y. Cai, C. Ma, Y. Zhu, J. X. Wang and R. R. Adzic, *Langmuir*, 2011, **27**, 8540-8547.
54. Y. Sun, B. T. Mayers and Y. Xia, *Nano Lett.*, 2002, **2**, 481-485.
55. Y. Sun and Y. Xia, *Science*, 2002, **298**, 2176-2179.
56. Y. Sun, B. Mayers and Y. Xia, *Adv. Mater.*, 2003, **15**, 641-646.
57. Y. Hu, Q. Shao, P. Wu, H. Zhang and C. Cai, *Electrochem. Com.*, 2012, **18**, 96-99.
58. B. Ravel and M. Newville, *J. Synchrotron Radiat.*, 2005, **12**, 537-541.
59. C. C. Herrmann, G. G. Perrault and A. A. Pilla, *Anal. Chem.*, 1968, **40**, 1173-1174.
60. J. Durst, M. Lopez-Haro, L. Dubau, M. Chatenet, Y. Soldo-Olivier, L. Guétaz, P. Bayle-Guillemaud and F. Maillard, *J. Phys. Chem. Lett.*, 2014, **5**, 434-439.
61. F. Maillard, S. Schreier, M. Hanzlik, E. R. Savinova, S. Weinkauf and U. Stimming, *Phys. Chem. Chem. Phys.*, 2005, **7**, 385-393.
62. F. Maillard, M. Eikerling, O. V. Cherstiouk, S. Schreier, E. Savinova and U. Stimming, *Faraday Discuss.*, 2004, **125**, 357-377.
63. A. Ohma, K. Shinohara, A. Iiyama, T. Yoshida and A. Daimaru, *ECS Trans.*, 2011, **41**, 775-784.
64. X. Wang, R. Kumar and D. J. Myers, *Electrochem. Solid-State Lett.*, 2006, **9**, A225-A227.
65. S. G. Rinaldo, J. Stumper and M. Eikerling, *J. Phys. Chem. C*, 2010, **114**, 5773-5785.
66. S. G. Rinaldo, W. Lee, J. r. Stumper and M. Eikerling, *Electrochem. Solid-State Lett.*, 2011, **14**, B47.
67. P. Strasser, *Rev. Chem. Eng.*, 2009, **25**, 255-295.
68. R. Callejas-Tovar and P. B. Balbuena, *J. Phys. Chem. C*, 2012, **116**, 14414-14422.
69. A. Schlapka, M. Lischka, A. Groß, U. Käsberger and P. Jakob, *Phys. Rev. Lett.*, 2003, **91**, 016101.
70. M. Lischka, C. Mosch and A. Groß, *Electrochim. Acta*, 2007, **52**, 2219-2228.

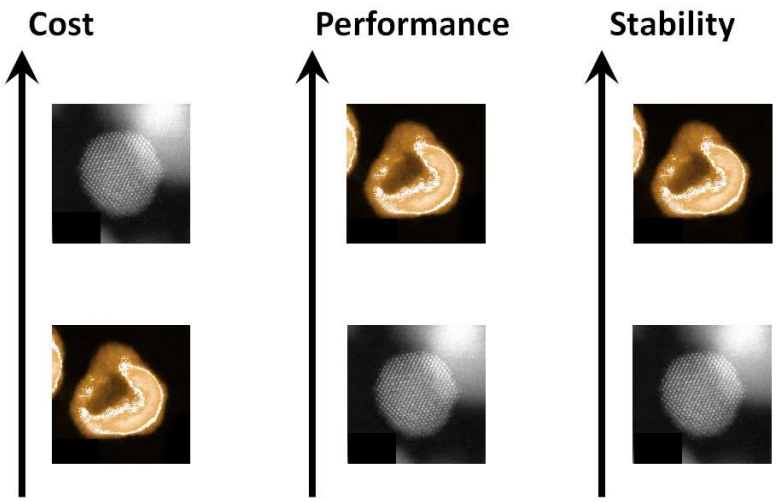

The hollow Pt_xNi_{1-x}/C nanocrystallites are capable of fulfilling cost, electrocatalytic performance, and durability requirements of proton-exchange membrane fuel cell applications.